5.5 DUAL-DOPPLER LIDAR MEASUREMENTS OF FLOW OVER A SUBURBAN AREA

Rob Newsom*[,1], Ron Calhoun[2], David Ligon[3], Jerry Allwine[1]

[1]Pacific Northwest National Laboratory, Richland, WA

[2]Department of Mechanical and Aerospace Engineering, Arizona State University, Tempe, AZ

[3]Army Research Laboratory, Adelphi, MD

1. INTRODUCTION

Dual-Doppler lidar observations are used to investigate the structure and evolution of surface layer flow over a suburban area. The observations were made during the Joint Urban 2003 (JU2003) field experiment in Oklahoma City in the summer of 2003. This study focuses specifically on a ten hour sequence of scan data beginning shortly after noon local time on 7 July, 2003. During this period two coherent Doppler lidars performed overlapping low elevation angle sector scans upwind and south of Oklahoma City's central business district (CBD). Radial velocity data from the two lidars are processed to reveal the structure and evolution of the horizontal velocity field in the surface layer throughout the afternoon and evening transition periods.

The retrieved velocity fields clearly show a tendency for turbulence structures to be elongated in the direction of the mean flow throughout the entire ten hour study period. As the stratification changed from unstable to weakly stable the turbulence structures became increasingly more linearly organized, and the spanwise separation between low speed "streaks" decreased. Estimates are given of the streamwise and cross-stream dimensions of these linearly organized turbulent structures as a function of stability.

This study also investigates the response of the velocity fields to the CBD and surrounding suburban area. For neutral and weakly stable stratification the retrievals show the effects of blocking due to the high concentration of tall buildings within the CBD. The retrievals also show a reduction in the wind speed on the order of 10%, and a counterclockwise turning of the winds over a broad area extending several hundred meters upwind of the CBD. The observed deviation in the wind direction is consistent with a cyclonic rotation caused by increased drag over the CBD and surrounding suburban area.

This paper is organized as follows. Section 2 briefly describes the JU2003 experiment and the instrumentation that is used in this study. Section 3 describes lidar data quality control and the methods that are used to retrieve surface layer winds from the dual-Doppler lidar data. Section 4 presents results of the dual-Doppler analysis, and a summary is given in section 5.

2. INSTRUMENTATION

The Joint Urban 2003 (JU2003) experiment was conducted in Oklahoma City, Oklahoma, during the period from June 28 to July 31, 2003 (Allwine et al. 2004). Participants included investigators from government laboratories, universities and the private sector. The main experimental objective was to provide much needed high-resolution dispersion (transport and diffusion) data at scales of motion ranging from flows in and around a single city block to the scale of the suburban area covering several kilometers around the CBD. A large number of instruments were deployed during JU2003. This study makes use of only those instruments shown in Fig 1. The main focus here is on the analysis of data from two coherent Doppler lidars. Supporting observations are provided by two radar profilers, radiosondes, and a surface energy balance tower.

2.1 Supporting Observations

Two 915 MHz radar profilers were deployed at sites north and south of the CBD. The profiler at the northern site was operated by Argonne

* *Corresponding author address*: Rob K. Newsom, Pacific Northwest National Laboratory, P.O. Box 999, MSIN K9-30, Richland, WA 99352; e-mail: rob.newsom@pnl.gov

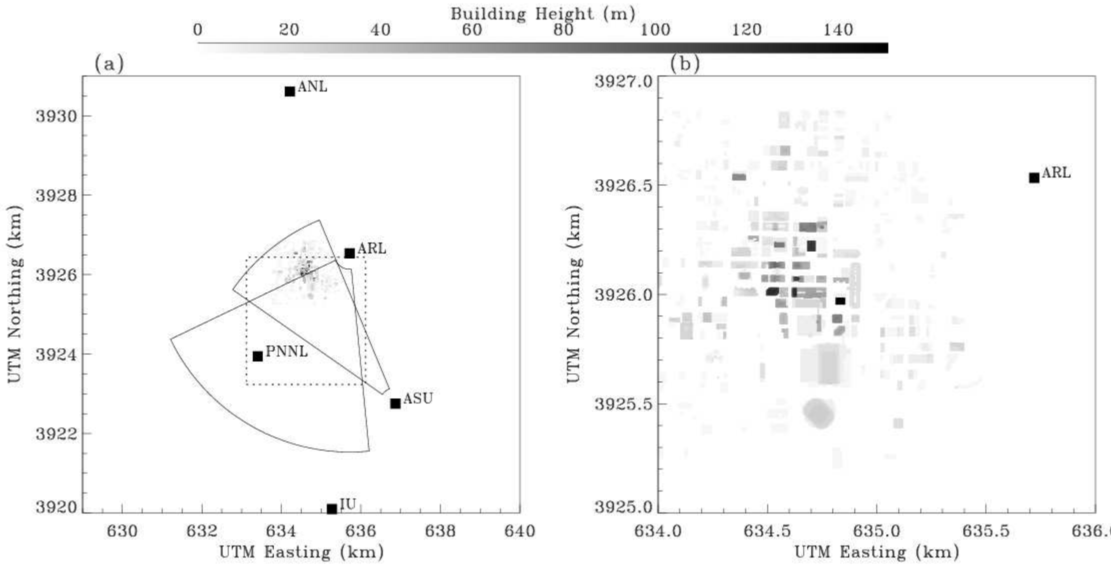

Figure 1. (a) Map showing the locations of the ARL lidar, ASU lidar, PNNL radar profiler, ANL radar profiler, and one of the IU energy balance towers. The dual-Doppler analysis domain is indicated by the dashed line in (a). (b) Building heights in the CBD and the ARL lidar. Mean building height is 18 m. The center of the CBD is located at x=635 km, and y = 3926 km, based on a building-height weighted average. Maps coordinates are based on a UTM projection with the WGS-84 datum.

National Laboratory (ANL), and the profiler at the southern site was operated by Pacific Northwest National Laboratory (PNNL). The PNNL site was located about 2 km south of the CBD, and the ANL site was located approximately 5 km north of the CBD. Both of these instruments provided 30 minute-averaged wind profiles continuously through the course of the entire experiment (De Wekker et al. 2004).

Radiosondes were launched from the two radar profiler sites (PNNL and ANL) and from another site operated by the Army Research Laboratory (ARL). The ARL radiosonde site was located immediately north of the CBD. Radiosondes were launched from the PNNL site at two hour intervals during IOPs, and once per day from the ARL site. Sondes provided measurements of air pressure, air temperature, relative humidity, wind speed, wind direction.

The University of Indiana (IU) conducted surface energy budget measurements at seven sites along a north-south axis, 5.5 to 6.5 km south of the CBD. For this study we use sonic anemometer data from the northern most site to characterize the inflow surface layer stability. More specifically, this study uses data from the TM4 sonic that was deployed at a height of 19.35 m AGL on the Tyler Media Group tower (Grimmond et al. 2004).

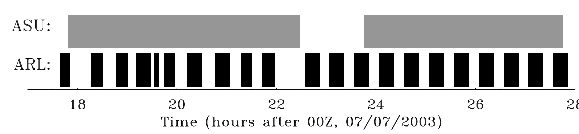

Figure 2. Temporal coverage of the low-elevation-angle sector scans. The gray bars indicate the temporal coverage for the ASU lidar, and the black bars indicate the temporal coverage for the ARL lidar.

2.2 Lidar

Researchers from Arizona State University and the US Army Research Laboratory (ARL) deployed two coherent Doppler lidars during JU2003. The ARL lidar was located atop a parking garage, approximately 1.4 km east-northeast of the CBD. The ASU lidar was deployed approximately 4 km to the south-southeast of the ARL lidar. Both of these lidars operated nearly continuously during IOPs, and episodically during non-IOPs. A variety of scan patterns were employed. Scanning strategies were coordinated between the two lidars in order to capitalize on the opportunity to acquire dual-Doppler data.

Both the ARL and ASU lidars were manufactured by CLR Photonics (CLR Photonics, Inc., 2002), and are nearly identical in their designs. These instruments employ solid state laser transmitters operating at a wavelength of 2μm, with a 400 ns (60 m) 2 mJ pulse, at a pulse repetition frequency (PRF) of 500 Hz. The software interface allows the operator to adjust many of the signal processing parameters. For the period examined in this study both lidars were configured with nearly identical signal processing parameters. Raw return signals were processed with 66-m range gates. The gate spacings for the ARL and ASU lidars were 66 m and 69 m, respectively. Each range resolved profile, or beam, was obtained by averaging 100 pulses. As a result, the beam rate, which is the PRF divided by the number of pulses averaged, was 5 Hz for both lidars.

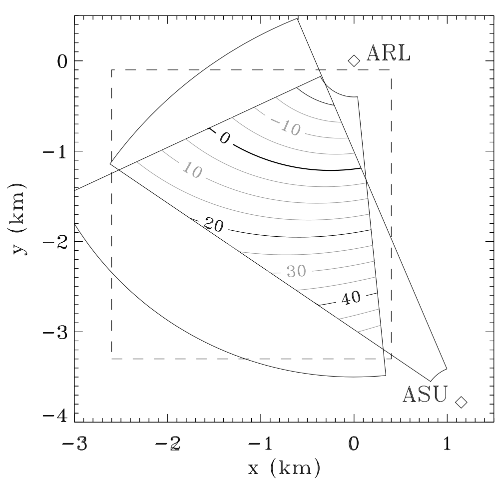

Figure 3. Height difference between the ARL and ASU low-elevation-angle sector scans. Maximum altitude difference is 57 m, the mean altitude is 32 m, and the mean absolute altitude difference is 16 m. The dual-Doppler analysis domain is indicated by the dashed line.

In this study we analyze observations from a series of lidar scans that were acquired between 1748 UTC on 7 July 2003 (1248 CDT) to 0345 UTC on 8 July, 2003 (2245 CDT on 7 July, 2003). During this period the ASU lidar performed only low elevation angle sector scans at an elevation angle of 0.5^o, in a 32.5^o arc toward the northwest between azimuths 305^o and 337.5^o. The scan rate was 2^o s^{-1}, so that each sector scan required about 16 seconds to complete. The ARL lidar was programmed to cycle through a sequence of different scan types every 30 minutes during this period. During each 30 minute cycle the ARL performed low elevation angle sector scans for about 20 minutes. The remaining ten minutes of each cycle were spent doing full PPI scans at elevation angles of 5^o and 25^o in order to acquire vertical profiles of mean winds. During the low elevation angle sector scans the ARL scanned a 70^o arc toward the south-southwest at and elevation angle of 1.2^o, between azimuths 174^o and 244^o. The scan rate was 5^o s^{-1}, so that each sector scan required about 14 s to complete. The area coverage for the low elevation sector scans are indicated in Fig 1. The temporal coverage of the low elevation sector scans for each lidar is illustrated in Fig 2. This figure shows when the scans overlap temporally.

Since the ARL and ASU scanned with slightly different elevation angles, the surfaces defined by their scans intersect only along a line. Figure 3 displays the height difference between the two lidar scan planes. Positive (negative) values indicate that the ARL (ASU) scan plane is above the ASU (ARL) scan plane. The scan planes intersect along an arc to the immediate south of the CBD. The ARL scan plane lies below the ASU scan plane to the north of this arc. A maximum height difference of near 57 m occurs closest to the ASU lidar. The mean absolute height difference over the over lap region is 16 m, and the mean height of the overlap region is 32 m.

The height difference between the ASU and ARL scan plane will have an impact on the retrieval of horizontal velocities. The retrieval method assumes that the scan planes are coaligned, or that the change in the horizontal velocity field with height is negligible. The retrievals produced from these dual-Doppler scans are thus assumed to be representative of a layer whose height is given by the mean height of the overlap and whose thickness is given by the mean height difference between the two scan planes within the overlap region.

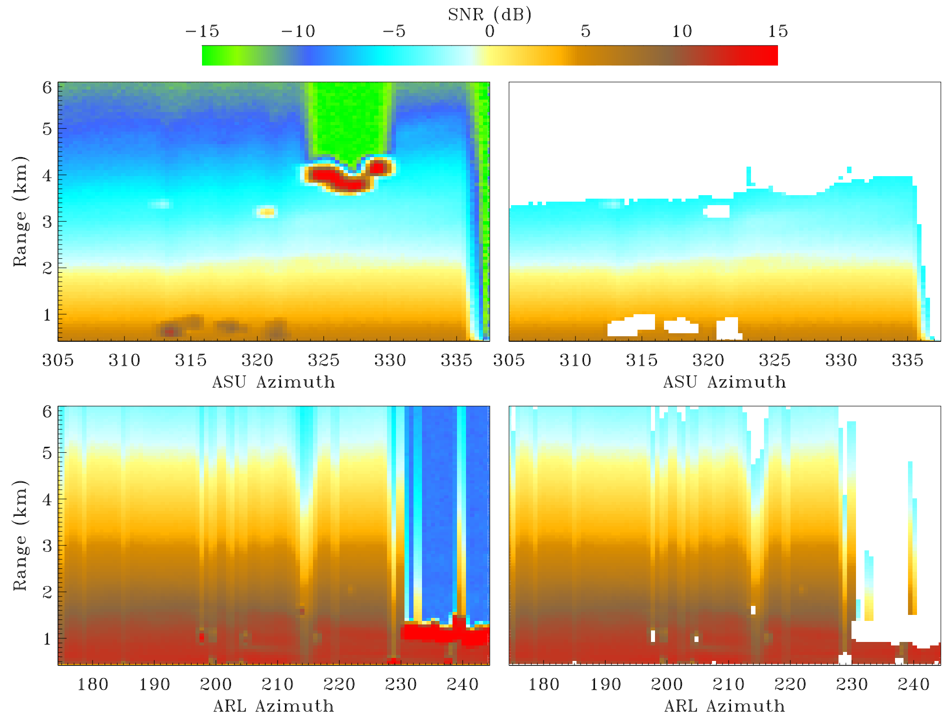

Figure 4. (a) The mean SNR as a function of range and azimuth for the low-elevation-angle sector scans from the ASU lidar. (b) The mean ASU SNR with the hard target mask applied. (c) The mean SNR as a function of range and azimuth for the low-elevation-angle sector scans from the ARL lidar. (d) The mean ARL SNR with the hard target mask applied.

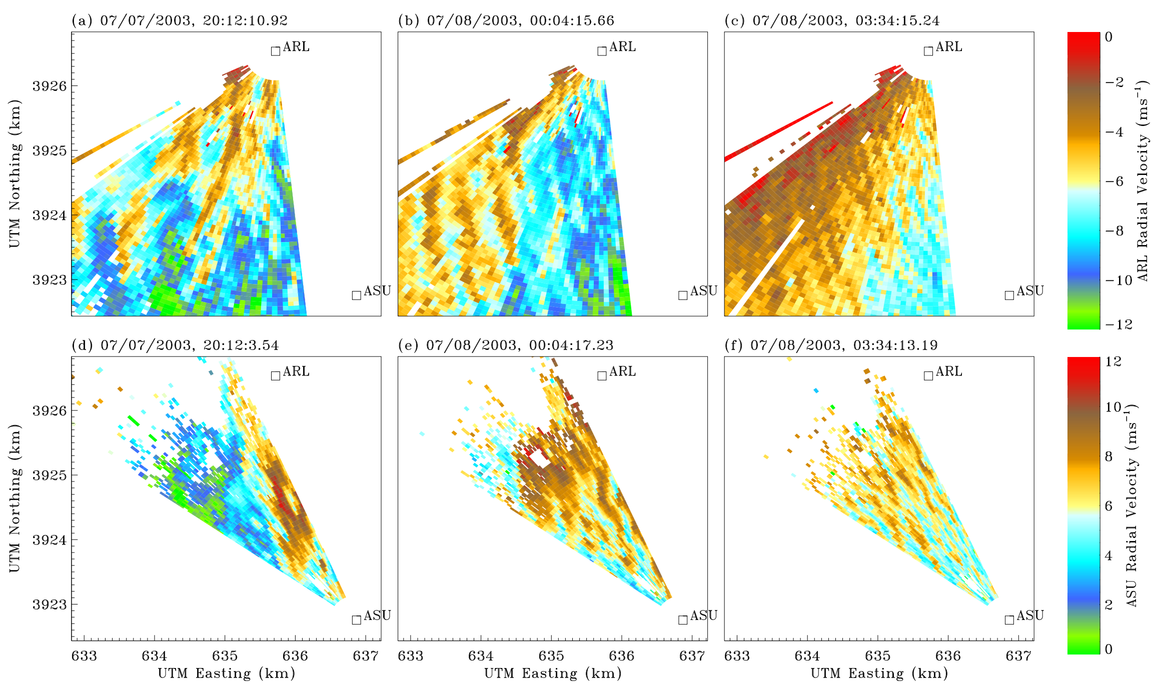

Figure 5. Representative samples of radial velocity data after QC processing. Panels (a) through (c) show ARL lidar data at three selected times. Panels (d) through (f) show ASU lidar data corresponding to the same times as the ARL data.

3. LIDAR ANALYSIS METHODS

This section describes the techniques that were applied to perform quality control of the ARL and ASU lidar data. The dual-Doppler wind retrieval algorithm is also described.

3.1 Lidar data quality control

Quality-control (QC) algorithms were used to identify and flag radial velocity measurements with low signal-to-noise ratios (SNR), and stationary hard targets (HTs). A prescribed minimum SNR threshold level was used to identify weak signals. Radial velocity measurements corresponding to SNR values falling below this threshold were flagged as missing. The detection of HTs, however, presented a more challenging problem.

Hard target returns are those signals resulting from backscatter from features such as buildings, trees, power polls, terrain, etc. These signals can be identified as spikes in the SNR field, with radial velocities close to zero (within the measurement error). However, HT detection is complicated by the range dependence of the SNR field. As a result, a simple thresholding approach based on a maximum prescribed SNR is generally not effective. Furthermore, SNR spikes due to HTs are often not confined to a single range gate. The return from a solid feature can "bleed" over into adjacent range gates due to the extended shape of the laser pulse. If these returns are not properly identified and rejected they can artificially bias the retrieved velocity toward zero in the vicinity of the feature.

Hard target detection is best handled on a case-by-case basis. In the present case, the lidars were performing repeated low elevation-angle sector scans. The HT detection algorithm employed in this study takes advantage of the fact that HTs appear at roughly the same azimuth angles on each scan pass.

For each lidar the average SNR field was computed as a function of azimuth and range. The result of this averaging process is shown in Fig 4. This figure illustrates how regions that are affected by HT returns can be easily identified visually. These regions were then hand edited using interactive software specifically developed for this purpose. The result of this editing process (also shown in Fig 4) was used to define a HT mask. The HT mask was then applied to the low-elevation-angle sector scan data. The end result of all QC processing is shown in Fig 5. This figure shows samples of radial velocity sector scan data after QC processing at three selected times.

3.2 Algorithm Description

The wind retrieval algorithm uses radial velocity data from the ARL and ASU lidars to estimate the horizontal velocity field within the dual-Doppler overlap area. The first step in the process is to define an analysis domain, as shown in Figs 1 and 2. The domain was chosen in order to completely enclose the area of over lap between the two scans. A Cartesian grid was then defined within this domain. A time grid was also defined by dividing the entire period from 1748 UTC on 7 July, 2003 to 0345 UTC on 8 July, 2003 into 30 second intervals. The retrieval algorithm assumes that the velocity field is locally homogeneous about a given node in the grid and constant within each 30 second time interval.

The horizontal velocity at a grid point within the dual-Doppler overlap area at time t is estimated by selecting a subset of measurements that satisfy

$$\left|\mathbf{r}-\mathbf{r}_n\right| < R_{\mathrm{inf}} , \tag{1}$$

and

$$\left|t-t_n\right| < \Delta t/2 , \tag{2}$$

where $\mathbf{r}$ is the position vector of a grid point within the analysis domain, t is the analysis time, $\mathbf{r}_n$ is the position vector of an observation, R_{inf} is a prescribed radius of influence, t_n is the time of an observation, and Δt is the temporal resolution of the analysis time grid. The horizontal velocity field is assumed to be homogeneous within the radius of influence, R_{inf}, and constant within Δt. For this analysis we used $R_{\mathrm{inf}} = 100\ m$ and $\Delta t = 30\ s$. The local horizontal velocity field is found by minimizing the following cost function:

$$J = \sum_n \left(\mathbf{u} \cdot \hat{\mathbf{r}}_n - u_{rn} \right)^2 , \tag{3}$$

where $\hat{\mathbf{r}}_n$ is a unit vector from the lidar to a radial velocity measurement, u_{rn} is the radial velocity measurement, and **u** is the horizontal velocity at **r** and *t*, i.e. $\mathbf{u} = (u, v, 0)$. Each radial velocity measurement has associated with it a beam azimuth, position vector and time tag. The summation in equation (3) is carried out over all measurements that satisfy the inequalities in (1) and (2). The unit vector $\hat{\mathbf{r}}_n$ can be expressed in terms of the beam azimuth, ϕ_i ,

$$\hat{\mathbf{r}}_i = \left(\sin\phi_i , \cos\phi_i , 0 \right). \tag{4}$$

Minimizing *J* with respect to *u* and *v* ($\partial J / \partial u = 0$, $\partial J / \partial v = 0$) results in the following simple two-by-two linear system

$$\sum_{j=1}^{2} A_{ij} u_j = b_i \quad \text{for} \quad i = 1, 2 , \tag{5}$$

where

$$A_{11} = \sum_n \sin^2 \phi_n , \tag{6}$$

$$A_{12} = A_{21} = \sum_n \sin\phi_n \cos\phi_n , \tag{7}$$

and

$$A_{22} = \sum_n \cos^2 \phi_n . \tag{8}$$

The solution to equation (5) is given by

$$u = \frac{A_{22} b_1 - A_{12} b_2}{|\mathbf{A}|} , \tag{9}$$

and

$$v = \frac{A_{11} b_2 - A_{12} b_1}{|\mathbf{A}|} . \tag{10}$$

We emphasize that equations (9) and (10) are applied locally at a given grid point in the dual-Doppler overlap area, and at time *t*. The analysis described above is repeated for all grid points and all times.

Finally, we note that in the analysis presented above no distinction has been made regarding which observations come from which lidar. It is easy to show that if all the radial velocity measurements within the region defined by inequalities (1) and (2) are taken from the same lidar, i.e. the same azimuth, then the determinant of **A** is zero ($|\mathbf{A}| = 0$), and thus there is no solution to equation (5). Furthermore, if the angles between the various observations defined by inequalities (1) and (2) are small then the resulting linear system (equation 5) will be ill-conditioned. The retrieval algorithm *does* check to ensure that there is at least one measurement from each lidar within the region defined by inequalies (1) and (2). If this condition is not satisfied then **u** is reported as missing.

4. RESULTS

This section presents the results of the dual-Doppler analysis. In order to put these results in perspective, we first present measurements that characterize the boundary layer during the dual-Doppler period.

4.1 Mean Flow Characteristics

Vertical profiles of virtual potential temperature are shown in Fig 6. The first three soundings were launched from the PNNL radar profiler site, and the last sounding was launched from ARL RAOB site. The sounding acquired near 1600 UTC (1100 CDT) shows a developing convective boundary layer with a well defined mixed layer and a capping inversion near 1200 m AGL. The two soundings acquired at about 2000 UTC (1500 CDT) and 2200 UTC (1700 CDT), show the boundary layer structure at the height of the afternoon period. At this time the capping inversion is located at about 1800 m AGL. The next available sounding was taken by ARL at about 0600 UTC (0100 CDT).

Time series illustrating the evolution of the surface layer stability are shown in Figure 7. This figure displays estimates of the friction velocity, u_*, and the stability parameter,

$$\xi = -\frac{z}{L_L} = -\frac{\overline{w'\theta_v'}}{kg\overline{\theta}_v}u_* \quad . \tag{11}$$

The friction velocity and stability parameter were computed from 5 minute averages of the IU TM4 sonic anemometer data. A strong southerly to southwesterly flow persisted during the entire study period. Thus, values of u_* remained fairly steady in the range from about 0.6 to 1.2 ms^{-1} during this period. The largest (negative) values of the stability parameter occur between about 1800 UTC (1300 CDT) and 2200 UTC (1700 CDT). The transition from negative to positive values occurs near 0100 UTC (2000 CDT).

Time-height cross sections of the mean winds during the study period are shown in Fig 8. This figure displays comparisons of the mean winds derived from the ARL lidar, the PNNL profiler, and the ANL profiler. The overall agreement between the various results is good. These results show that, below about 1000 m AGL, the winds experience a slight shift in direction from the south-southwest to south-southeast during the study period.

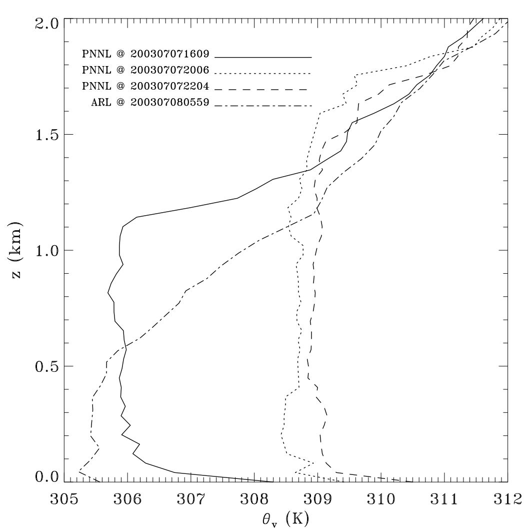

Figure 6. Profiles of virtual potential temperature from radiosondes launched during the study period. The solid, dotted and dashed curves are from soundings launched at the PNNL site at 1609, 2006, and 2204 UTC, respectively. The dash-dotted curve is a sounding launched from ARL raob site at 0600 UTC on 8 July 2003.

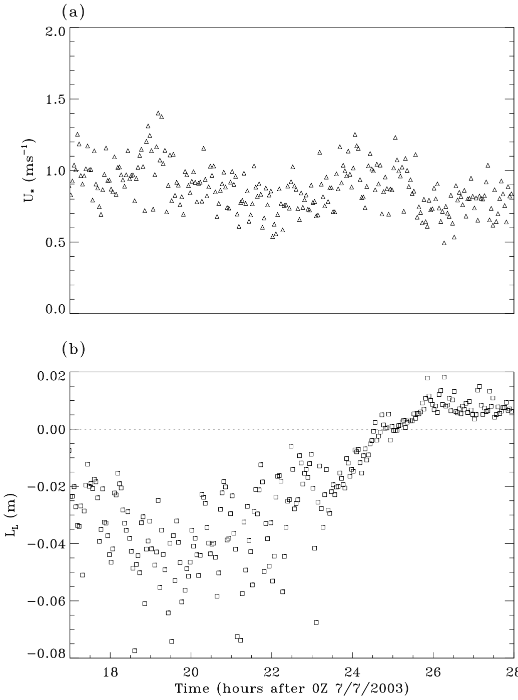

Figure 7. Time series of (a) U star, and (b) stability parameter z/L computed from 5 minute averages of the IU TM4 sonic anemometer data.

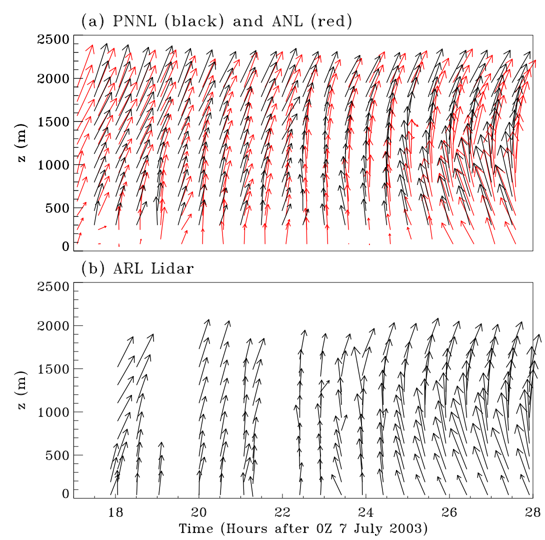

Figure 8. Comparisons between wind profiles from (a) the PNNL profiler (black), the ANL profiler (red), and (b) the ARL lidar. The vertical resolution has been degraded for both the radar profilers and the lidar for display purposes.

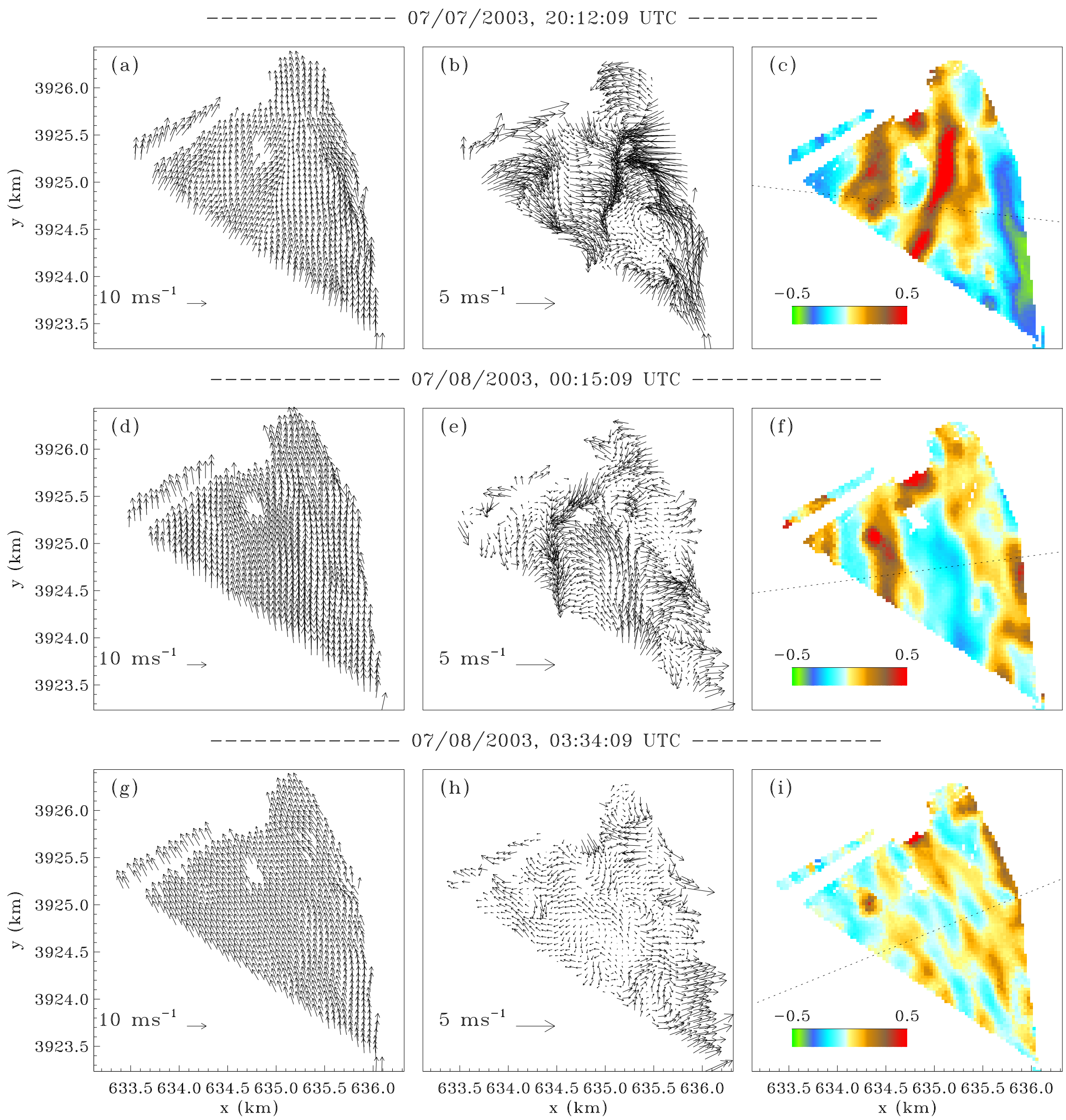

Figure 9. Horizontal velocity fields retrieved from the dual-Doppler lidar data. The left, middle, and right panels show $\mathbf{u}$, $\mathbf{u}'$ and η (equation 12), respectively. Panels (a) through (c) show these fields at 2012:09 UTC on 7 July 2003. Panels (d) through (f) show these fields at 0015:09 UTC on 8 July 2003. Panels (g) through (i) show these fields at 0334:09 UTC on 8 July 2003.

4.2 Retrieved Surface Layer Flow

Figure 9 shows representative samples of the retrieved velocity at three selected times. Figures 9a through 9c show the retrieved fields at 2012 UTC (1512 CDT) during the height of afternoon period when the boundary layer exhibited maximum instability. Figures 9d through 9f show the velocity fields at 0015 UTC (1915 CDT), just before the sensible heat flux changes from positive to negative (see Fig 7). Figures 9g through 9i show the velocity fields at 0334 UTC (2234 CDT), when the boundary layer is weakly stable.

The fields shown in Fig 9c, 9f, and 9i clearly indicate a tendency for turbulent eddies tend to form linearly organized structures. These structures are aligned, more or less, along the mean flow direction. Turbulent features become more linearly organized over the course of the study period. For the unstable case the linear organization is not nearly as obvious, because the structures are larger and the dual-Doppler over lap region has a limited extent. However, the linear organization *is* present and can be seen by examining animations of the retrievals over this period.

The linear structure of the flow is apparent in the wind speed as well other fields that can be derived from the velocity, such as the two-dimensional divergence, vertical vorticity fields, or the streamwise component of the velocity. We found that the linear structure is particularly apparent by accentuating the low speed regions. Figure 10c, 10f, and 10i show a derived parameter that accentuates the low speed regions of the flow. This parameter is defined as follows

$$\eta = \frac{u_o}{|\mathbf{u}|} - 1, \quad (12)$$

where

$$u_o = |\langle \mathbf{u} \rangle| \quad (13)$$

is the area averaged mean wind speed. It is clear that $\eta < 0$ for wind speed deviations greater than the mean, and that $\eta > 0$ for wind speed deviations less than the mean. Low speed regions delineated in this manner show a distinctly linear organization. The flow structures shown in Fig 9 are qualitatively similar to the structures observed in large-eddy simulations of neutral and shear-driven convective boundary layers (Moeng and Sullivan, 1994; Lin et al., 1996; Kim and Park, 2003).

There were also changes in the scale of the linear structures as the stability changed. As the stability increased the structures became more linear and the separation between low speed streaks decreased. In order to estimate the transverse separation between low speed streaks we computed the autocovariance of the streamwise velocity component as a function of displacement in the cross-stream direction. The normalized autocovariance function was defined as

$$R(\Delta x_\perp) = \frac{\left\langle u'_\parallel(x_\perp + \Delta x_\perp, t) u'_\parallel(x_\perp, t) \right\rangle}{\left\langle \left(u'_\parallel(x_\perp, t)\right)^2 \right\rangle} \quad (14)$$

where $u'_\parallel$ is the perturbation streamwise velocity component, $x_\perp$ is the coordinate orthogonal to the streamwise direction, and $\Delta x_\perp$ is the cross stream displacement. The angle brackets in equation (14) denote averaging over the transverse coordinate, $x_\perp$, and over time, *t*. Equation (14) was computed using a one-dimensional cross section of $u'_\parallel$ along a line orthogonal to the mean wind direction. The cross section was chosen to be far enough upstream of the CBD to avoid obvious build affects. These cross sections are shown by the dotted lines that transect the domain in Figs 10c, 10f and 10i.

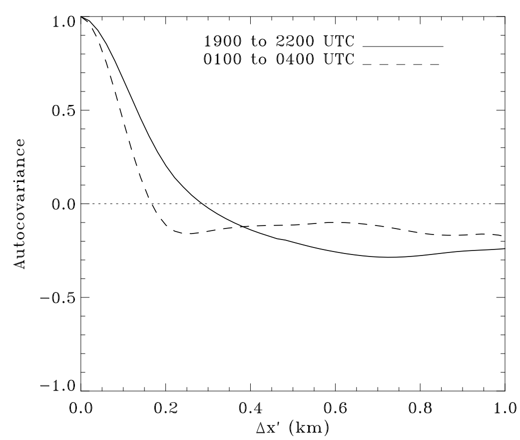

Figure 10. Autocovariance curves computed along line orthogonal to the mean flow averaged over two different periods. For the unstable period (1900 to 2200 UTC) the zero crossing occurs at 281 m and the first minimum occurs at 724 m. For the neutral/ weakly stable period (0100 to 0400 UTC) the zero crossing occurs at 161 m, and first Minimum occurs at 261 m.

Autocovariance curves corresponding to two distinctly different stability conditions are shown in Figure 10. The solid curve in Fig 10 was computed from equation (14) by averaging from 1900 to 2200 UTC (1400 to 1700 CDT) and is therefore representative of a shear driven convective boundary layer. The dashed curve in Fig 10 was computed by averaging from 0100 to 0400 UTC (2000 to 2300 CDT), when conditions were weakly stable. Both curves indicate distinct minima, corresponding to cross-stream displacements, $\Delta x_\perp$, for which the streamwise velocity becomes approximately anticorrelated. These cross-stream displacements, $\Delta x_{\perp}$, provide a rough measure of separation between high and low speed regions, or roughly half the distance between two adjacent low speed regions.

The covariance curve for the neurtal case exhibits a more well defined minimum. This is consistent with our general observations that the streaky structure becomes more well defined under near-neutral conditions. Estimates of the streak spacing degrade as the streak spacing increases due to the finite span of the observations. As the lag displacement increases the statistics degrade because fewer samples are used in the average. Thus, the estimates of streak spacing become less reliable under unstable conditions due to the larger separations.

Table 1 provides a summary of the autocovariance analysis. The results are tabulated with the average u_* and stability parameter, ξ, during the same period. This table shows the values of $\Delta x_{\perp}$ at R=0 and at the minimum of R. The mean cross-stream separation between low-speed streaks is estimated based on the value of $\Delta x_{\perp}$ at the minimum of R. The results shown in Table 1 imply that the streak spacing is approximately 1.4 km in the unstable case and 500 m in the weakly stable case.

Averaging Period		u_* (ms^{-1})	ξ	$\Delta x_{\perp}$ @	
UTC	CDT			R=0	Min(R)
1900-2200	1400-1700	0.89	-0.044	281	724
0100-0400	2000-2300	0.81	0.007	161	261

Table 1. Results of the autocovariance analysis. Columns 5 and 6 give the values of the cross-stream displacement, $\Delta x_{\perp}$, at R=0 and at the minimum of R, respectively.

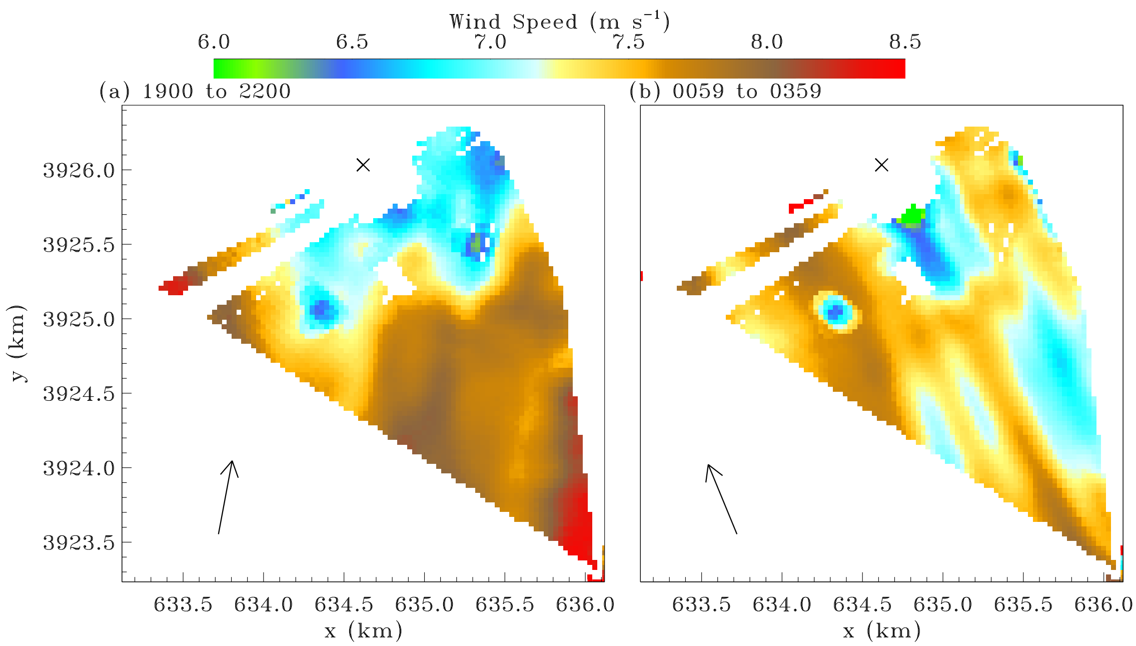

Figure 11. Mean wind speeds averaged from (a) 1900 to 2200 UTC 7 July 2003, and from (b) 0100 to 0400 UTC 8 July, 2003. The mean wind direction is indicated by the arrow. The center of the CBD is indicated by the X.

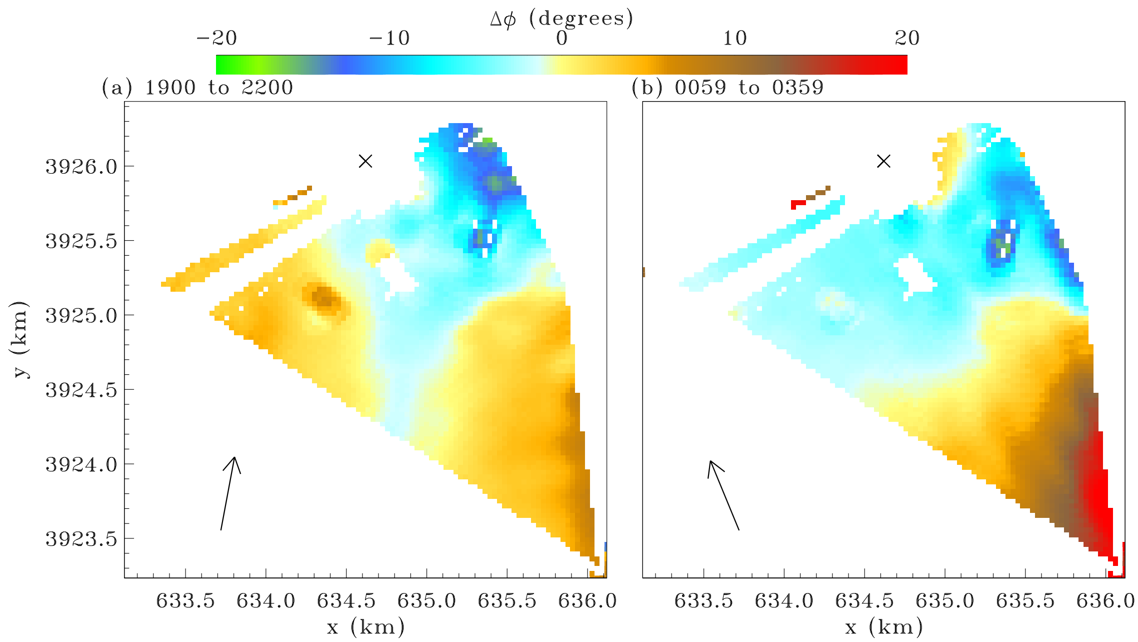

Figure 12. Deviation of the wind direction from the area averaged wind direction. Positive (negative) values indicate clockwise (counterclockwise) rotation. Mean wind directions are averaged from (a) 1900 to 2200 UTC 7 July 2003, and from (b) 0100 to 0400 UTC 8 July, 2003. The center of the CBD is indicated by the X.

4.3 CBD Effects on the Mean Flow

When individual frames of retrieved velocity fields are inspected it is difficult to discern the affect of the CBD on the upstream flow. It is only when appropriate averaging is applied that the effects become apparent. In order to examine how the upstream winds are affected by the CBD, the retrieved fields were averaged over the same two periods used in the autocovariance analysis above. Figure 11a shows the wind speed averaged from 1900 to 2200 UTC (1400 to 1700 CDT CDT 7 July) and Fig11b shows the average wind speed for the period from 0100 to 0400 UTC 8 July (2000 to 2300 CDT 7 July). It is clear that there is a significant reduction in the average wind speed in the upstream direction in both stability regimes.

In the unstable case (Fig11a) there appears to be a general decrease in wind speed from the southern most point in the dual-Doppler over lap area toward the CBD. However, the slowing is more abrupt within 1.0 km upstream of the CBD. Within this range the wind speed decreases by roughly 10%.

In the weakly stable case (Fig 11b), the affect of the CBD on the upstream wind speed appears to be more localized and more intense. A region of significantly lower wind speed extends for roughly 1 km immediately upstream of the CBD, with higher speed flow to either side of the CBD. Within 1 km immediately upstream of the CBD the wind speed decreases from 7.5 ms^{-1} to about 6 ms^{-1}, a decrease of approximately 25 %..

To investigate possible affects of the CBD on wind direction we found it helpful to display the time-mean wind direction relative to the time and area averaged wind direction. The wind direction deviation was defined to be

$$\Delta\phi = \tan^{-1}(\overline{u}/\overline{v}) - \tan^{-1}(\langle\overline{u}\rangle/\langle\overline{v}\rangle), \qquad (15)$$

where the overbar implies time averaging and the angle brackets imply area averaging. The first term on the right side of equation (15) is the time-mean vector direction at each point in the dual-Doppler over lap region. The second term is simply the overall mean vector direction. Positive (negative) values of $\Delta\phi$ indicate clockwise (counterclockwise) rotation relative to the mean wind direction.

Figure 12a displays the wind direction deviation averaged from 1900 to 2200 UTC (1400 to 1700 CDT CDT 7 July) and Fig12b shows the wind direction deviation for the period from 0100 to 0400 UTC 8 July (2000 to 2300 CDT 7 July). For the weakly stable case (Fig 13b), a small region of positive of $\Delta\phi$ is evident on the east side of the CBD. This suggests a bifurcation of the flow around the CBD in the horizontal plane, consistent with the type of motion expected under stable stratification. By contrast, this same effect is not observed in the unstable case (Fig 12a).

For both the weakly stable and unstable cases Fig 12 shows that there is a broad area of negative $\Delta\phi$ extending well upstream of the CBD. A possible explanation is that the flow experiences a cyclonic rotation due to a reduction in the Coriolis acceleration, which in turn is caused by increased drag over the CBD and surrounding suburban area (Bornstein and Johnson 1976). We note that Berg et al. (2004) also observed systematic wind direction shifts over Oklahoma City from an analysis of sodar data acquired during JU2003. In order to investigate this effect and to corroborate the retrieval results we examined profiles of mean wind speed and wind direction from the ARL lidar, ASU lidar, PNNL radar profiler, and the ANL radar profiler. The ARL lidar is located closest to the CBD, whereas the ANL profiler and the ASU lidar are located approximately equal distances north and south of the CBD, respectively (see Fig 1).

Figure 13 shows vertical profiles of the mean wind speed and wind direction from the two Doppler lidars and the two radar profilers. These profiles were obtained between 1700 and 1730 UTC on 7 July 2003. This was the closest time to the study period that the ASU lidar performed scans appropriate for deriving mean wind profiles. We observe that there is good agreement between wind direction profiles from the PNNL profiler and the two lidars. Unfortunately, no data is available from the PNNL profiler below about 280 m. The ASU lidar wind direction is approximately constant with height. Below 200 m the winds observed by the ARL lidar begin to diverge counterclockwise from the ASU winds. This confirms the results obtained from low-elevation angle dual-Doppler analysis, and suggests that there is a counterclockwise rotation of the winds over the city center relative to outlying areas.

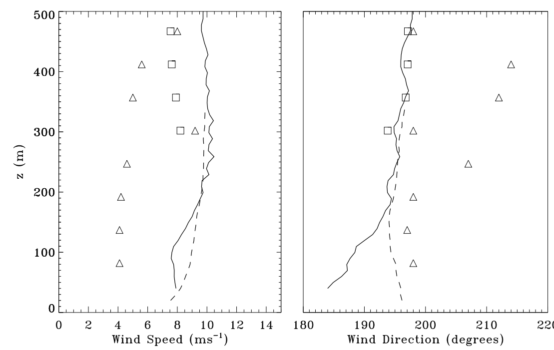

Figure 13. Comparison between mean wind (left), and wind direction (right) profiles from the ARL lidar (solid line), the ASU lidar (dashed line), the ANL radar profiler (triangles), and the PNNL radar profiler (squares). The times for each profile were chosen to be the closest available to the ASU data.

5. SUMMARY

This study presents an analysis dual-Doppler lidar data acquired during the JU2003 field program. Dual-Doppler observations were processed to reveal the structure and evolution of the horizontal velocity field in the surface layer upstream of the Oklahoma City CBD. The retrieved velocity fields clearly show a tendency for turbulence structures to be elongated in the direction of the mean flow. This tendency for linear organization became more apparent as the stratification changed from unstable to weakly stable. The transverse separation between low speed regions was estimated to be 1.4 km in the shear driven convective boundary layer, and about 500 m in the weakly stable case. Future work will include estimation of the streamwise extent of these structures. This information can be used to determine the aspect ratio and how that ratio changes with stability.

This study also investigated the response of the mean upstream flow to the CBD. In the unstable case the dual-Doppler retrievals show a decrease in wind speed from the southern most point in the dual-Doppler over lap area toward the CBD. The slowing is most abrupt within 1.0 km upstream of the CBD. Within this range the wind speed decreases by roughly 10%. In the weakly stable case the slowing is more intense and more concentrated immediately upstream of the CBD. Within 1 km immediately upstream of the CBD the wind speed decreased by approximately 25 %. The retrievals also indicate a channeling of the flow around the CBD in the weakly stable case. This effect is not observed in the unstable case.

The wind retrievals indicate a significant counterclockwise rotation in the wind direction over a broad area extending upwind of the CBD. It is suggested that this rotation is caused by a reduction in the Coriolis acceleration over the CBD and surrounding suburban area as a result of increased drag. A preliminary analysis of independent measurements appears to confirm these observations. However, a more comprehensive investigation should be performed to determine if this effect is observed on other days. Future work will incorporate observations from a network of sodars deployed at varying distances from the CBD (Berg et al. 2004).

Acknowledgements. The authors express their gratitude to the members of PNNL profiler and raob team, the ARL lidar and raob team, ASU lidar team, the ANL profiler team, and the IU team. We also wish to thank the organizers of the JU2003 field experiment and Dugway Proving Grounds for maintaining the JU2003 database and the web interface.

References

Allwine, K.J., M.J. Leach, L.W. Stockham, J.S. Shinn, R.P. Hosker, J.F. Bowers, and J.C. Pace, 2004: Overview of Joint Urban 2003 - An atmospheric dispersion study in Oklahoma City. Preprint, *Symp. Planning Nowcasting and Forecasting in the Urban Zone*, Seattle, WA, Amer. Meteor. Soc., CD-ROM, J7.1.

Bornstein, R.D., and D.S. Johnson, 1976: Urban-rural wind velocity differences. *Atmos. Env.*, **11**, 597-604.

CLR Photonics, Inc., 2002: *WindTracer System Operation and User Manual*. CLR Photonics, Inc., P.O. Box 7488, Boulder, CO USA 80306.

Berg L.K., et al., 2004: Observations of boundary-layer winds in an urban environment. *AMS 5th Conf. on Urban Environment.* Vancouver, B.C., Canada, 23-27 August 2004.

De Wekker S.F.J., et al., 2004: Boundary-layer structure upwind and downwind of Oklahoma City during the Joint Urban 2003 field study. *AMS 5th Conf. on Urban Environment.* Vancouver, B.C., Canada, 23-27 August 2004.

Grimmond, C.S.B.,et al., 2004: Variability of sensible heat fluxes in a suburban area of Oklahoma City. *AMS Symposium on Planning, Nowcasting, and Forecasting in the Urban Zone*. Seattle, WA, 12-15 January 2004.

Kim, S.W., and S.U. Park, 2003: Coherent structures near the surface in a strongly sheared convective boundary layer generated by large-eddy simulation. *Bound.-Layer Meteor.*, **106**, 35-60.

Lin, C-L, J.C. McWilliams, C-H Moeng, P.P. Sullivan, 1996: Coherent structures and dynamics in a neutrally stratified planetary boundary layer flow. *Phys Fluids*, **8**, 2626-2639.

Moeng, C-H., and P. P. Sullivan, 1994: A comparison of shear- and buoyancy-driven planetary boundary layer flows. J. Atmos. Sci., 51, 999-1022.